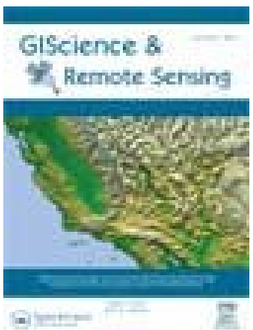

GIScience & Remote Sensing

ISSN: 1548-1603 (Print) 1943-7226 (Online) Journal homepage: http://www.tandfonline.com/loi/tgrs20

Snowmelt detection from QuikSCAT and ASCAT satellite radar scatterometer data across the Alaskan North Slope

Emily J. Sturdivant, Karen E. Frey & Frank E. Urban

To cite this article: Emily J. Sturdivant, Karen E. Frey & Frank E. Urban (2018): Snowmelt detection from QuikSCAT and ASCAT satellite radar scatterometer data across the Alaskan North Slope, GIScience & Remote Sensing, DOI: 10.1080/15481603.2018.1493045

To link to this article: https://doi.org/10.1080/15481603.2018.1493045

GIScience & Remote Sensing, 2018
https://doi.org/10.1080/15481603.2018.1493045

Snowmelt detection from QuikSCAT and ASCAT satellite radar scatterometer data across the Alaskan North Slope

Emily J. Sturdivant [a,b], Karen E. Frey*[a] and Frank E. Urban[c]

[a]*Graduate School of Geography, Clark University, Worcester, MA 01610, USA;* [b]*Woods Hole Coastal and Marine Geology Science Center, U.S. Geological Survey, Woods Hole, MA, 02543, USA;* [c]*Geosciences and Environmental Change Science Center, U.S. Geological Survey, Lakewood, CO, 80225, USA*

(*Received 24 January 2018; accepted 16 June 2018*)

The timing of seasonal snowmelt in high-latitude tundra has implications ranging from local biological productivity to global atmospheric circulation, yet remains difficult to quantify, particularly at large spatial scales. Snowmelt detection in such remote polar environments is possible using satellite-based microwave scatterometers, such as NASA's QuikSCAT. QuikSCAT measured scattering in Ku-band, which is sensitive to snowmelt signals, from 1999 until the antenna failed in 2009. The Advanced Scatterometer (ASCAT) (2006–2021 (*projected*) operational), which operates at C-band, may be able to extend the QuikSCAT record, but existing techniques fail to adequately monitor tundra environments. Here, we designed a departure threshold algorithm to produce a consistent 15-year time series of melt onset for the tundra of the Alaskan North Slope, using the overlap period for the enhanced resolution datasets to calibrate the ASCAT melt detection record against QuikSCAT. We produced a time series of day of year of melt onset for 4.45 km x 4.45 km grid cells on the Alaskan North Slope from 2000–2014. Time series validation with *in situ* mean daily air temperature produced mean R^2 values of 0.75 (QuikSCAT) and 0.72 (ASCAT). We qualitatively observed a difference between early-season melt, which occurred rapidly and was driven by strong wind events, and more typical melt, which occurred gradually along a latitudinal gradient. We speculate that future melt timing will have greater frequency of early-season onset as climate change destabilizes the high-latitude atmosphere.

Keywords: snowmelt; Alaskan North Slope; scatterometer; QuikSCAT; ASCAT; melt detection

1. Introduction

The last several decades have seen disproportionate warming in the Arctic, where the primary control on air temperatures is seasonal snow cover (IPCC 2014). The seasonal duration of Northern Hemisphere snow cover has decreased 5.3 days per decade since winter 1972–1973 (IPCC 2014), with the greatest rates of decrease at higher latitudes (Déry and Brown 2007). These declines in seasonal duration of Arctic snow cover are attributed to earlier spring snowmelt (Saito et al. 2013; Callaghan et al. 2011; IPCC 2014). Over the last 40 years, June high-latitude snow cover has decreased at a rate greater than the loss of September sea ice extent in the Arctic (IPCC 2014). The timing of seasonal melt onset at high-latitude tundra has implications ranging from local biological

*Corresponding author. Email: kfrey@clarku.edu

productivity to global atmospheric circulation (Male and Granger 1981; Eugster et al. 2000; Stone et al. 2002; Zhou et al. 2014). In particular, snowmelt affects global energy dynamics, surface water hydrology, permafrost stability, and ocean circulation (Male and Granger 1981; Stone et al. 2002).

Climate models and extrapolations have been used to calculate melt trends, but they offer only a coarse understanding of snowmelt dynamics. High-latitude changes, particularly in terrestrial snow cover, are poorly documented empirically and have coarse spatial resolutions or spatially dispersed measurements (IPCC 2014). As described in the fifth IPCC assessment report (WG1 AR5 Chapter 4, IPCC 2014), "long-duration, consistent records of snow are rare owing to many challenges in making accurate and representative measurements." A robust time series of precise snowmelt onset across the Arctic could provide insights into the feedbacks between climate and Arctic snowpack, which would aid future climate projections. However, remote locations and harsh climate impede comprehensive direct measurements; meteorological stations are poorly distributed and *in situ* measurements are lacking (IPCC 2014).

Well-calibrated satellite radar scatterometer data are an alternative to ground-based measurements. They can detect surface moisture at high temporal resolution over broad spatial extents without pollution from clouds or reliance on solar conditions (Ulaby et al. 1981). Scatterometers measure decibels (dB) of backscatter, calculated as the ratio of emitted energy to received energy. Resultant backscatter datasets are often applied to melt detection in cryospheric systems because backscatter is sensitive to even small amounts of liquid in snowpack owing to the dielectric properties of water (Ulaby et al. 1981; Bartsch, Wagner, and Naeimi 2010). Backscatter signals from tundra systems tend to be noisy given their heterogeneous moisture and landform composition (Howell et al. 2012).

An effective sensor for the precise detection of tundra snowpack transitions is NASA's Quick Scatterometer (QuikSCAT), a Ku-band radar scatterometer with a decadal (1999–2009) mission lifespan (Long and Hicks 2010). Ku-band is sensitive to moisture, which enables the use of QuikSCAT for time series analysis of freeze-thaw transitions for pan-Arctic tundra (Howell et al. 2012; Mortin et al. 2012). In November 2009, QuikSCAT's rotating antenna failed, which stalled the freeze-thaw record, given the scarcity of comparable sensors. The Scatterometer Image Reconstruction (SIR), part of the NASA Scatterometer Climate Record Pathfinder project (SCP) (Hicks and Long 2006), provides enhanced resolution backscatter images with a standardized grid system.

The C-band Advanced Scatterometer (ASCAT) has the greatest potential to extend the QuikSCAT record because their mission lifespans overlap and C-band backscatter resembles Ku-band in its sensitivity to moisture in the snowpack (Bartsch et al. 2010; Mortin et al. 2014). The SIR enhanced resolution product of ASCAT begins in January 2009 and is projected to continue beyond 2020 (Lindsley and Long 2010a; Wagner et al. 2013). While progress has been made to extend snowmelt records for sea ice using ASCAT and QuikSCAT (Mortin et al. 2014), consistent multi-year records of tundra snowmelt onset are currently lacking. Furthermore, there are no previous studies that conduct a direct comparison between QuikSCAT and ASCAT for terrestrial melt detection.

In this study, we demonstrate that ASCAT can be used to extend the QuikSCAT record of melt detection for seasonally snow-covered tundra. We detect annual snowmelt onset for the tundra of the Alaskan North Slope using a departure from running median algorithm applied to time series of both QuikSCAT and ASCAT. To measure the consistency between datasets, we compare QuikSCAT and ASCAT snowmelt onset timing in 2009 with *in situ* and reanalysis air temperature. We produce a time series of day of year

of melt onset for each 4.45 km x 4.45 km grid cell on the North Slope from 2000–2014 (QuikSCAT 2000–2009 and ASCAT 2010–2014). We then evaluate the spatial and temporal patterns of melt events and the context of future climate scenarios.

2. Study area

The Alaskan North Slope is a region of continuous permafrost bounded by the Brooks Range to the south and the Chukchi and Beaufort Seas to the northwest and northeast, respectively (Figure 1). The Brooks Range isolates the North Slope from the rest of the continent and descends northward into the Brooks Foothills ecoregion, a rolling upland of low shrub and tussock tundra (Kittel et al. 2011). The Beaufort Coastal Plain (BCP) ecoregion, an expansive coastal lowland (mean elevation 28 m) that is considered 82% wetland, gradually rises from the ocean to the Brooks Foothills. North Slope mean air temperatures are below freezing from September through May (Arp and Jones 2009). The BCP receives approximately 130 mm yr^{-1} of precipitation, of which 20 mm falls during winter and spring (Arp and Jones 2009). The mean annual precipitation at Umiat, a representative site in the Brooks Foothills is 139 mm (WRCC 2003). Precipitation rates

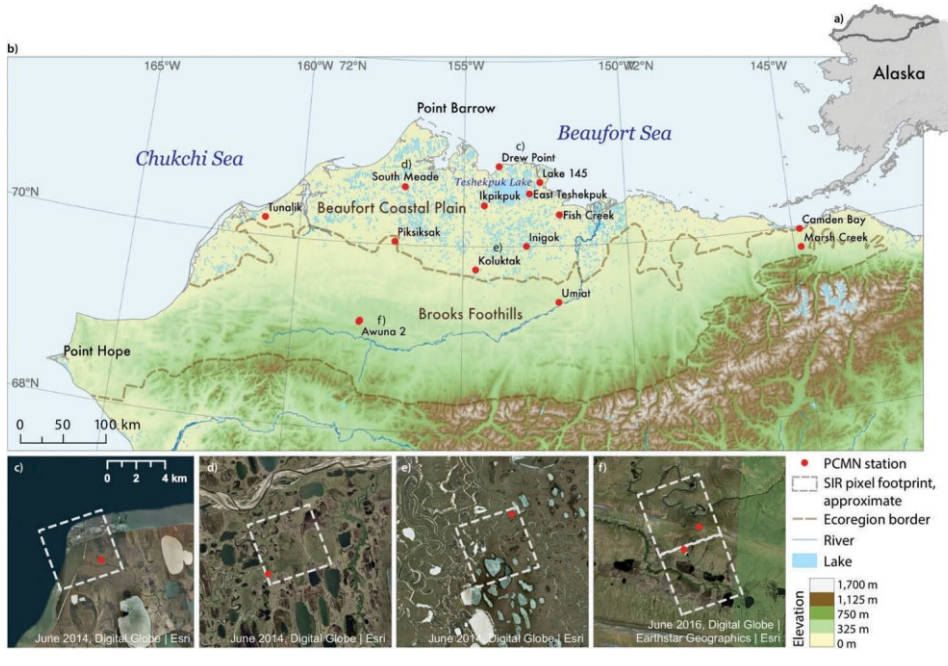

Figure 1. The Alaskan North Slope study area, outlined in gray in panel (a) and displayed in panel (b). The study area is composed of two ecoregions: Brooks Foothills and Beaufort Coastal Plain (labeled and delineated with brown dotted lines). Fourteen meteorological stations in the Permafrost and Climate Monitoring Network (PCMN) were used for ancillary data (red labeled points). The basemap is a digital surface model (DSM) overlaid by lake polygons and coastline (Jones and Grosse 2012). Four PCMN stations are used as examples in subsequent figures. They are labeled with letters that correspond to lower four panels and ordered by distance from the coast: c) Drew Point, d) South Meade, e) Koluktak, and f) Awuna 2. Dashed gray squares approximate the 4.45 x 4.45 km pixel footprints in the SIR grid system. Basemap imagery from DigitalGlobe was provided by Esri. All images were acquired in June.

and air temperature increase moderately from north to south into the Brooks Foothills (Wendler, Shulski, and Moore 2010). Likewise, snow depth tends to increase with both elevation and distance from the coast, although these patterns often deteriorate in the Foothills (Urban and Clow 2014). Observations at Inigok, a representative inland site on the BCP, suggest that snow depth often increases immediately before melt onset, which typically occurs over a 7–10 day period in late May or early June (Urban and Clow 2014). The winter temperature regime of the North Slope is dictated by passing weather systems, whereas the summer has a strong diurnal cycle corresponding to changes in incident solar radiation (Urban and Clow 2014). The Brooks Range limits the passage of southerly winds from the Pacific Ocean and tends to isolate the North Slope climate system from non-polar sources (June–September) (Kittel et al. 2011). The prevailing winds are easterly and are particularly strong along the coast where they also drive the Beaufort Gyre, an anticyclonic (i.e. clockwise) system of surface ocean currents that push ice and water from east to west along the coast. From fall through spring, low-pressure systems intensify in the Bering Sea and send gale force cyclonic winds toward the mainland (Shulski and Wendler 2007). Holistically, this suggests that detailed and accu- rate monitoring of the North Slope is particularly important given its role in regulating terrestrial, oceanic, and atmospheric systems.

3. Data

3.1 Satellite radar scatterometer

3.1.1. QuikSCAT

This study used radar backscatter time series data from SeaWinds on QuikSCAT and ASCAT on MetOp-A (Figure 2). The QuikSCAT satellite collected SeaWinds Ku-band (13.4 GHz frequency, 2.2 cm wavelength) backscatter measurements from June 1999 to November 2009 (Long and Hicks 2010). QuikSCAT collected more than six polar observations daily with a conically scanning pencil-beam antenna sending and receiving horizontally and vertically polarized Ku-band microwaves (Wang, Derksen, and Brown 2008). We used vertically polarized sent and received (VV-polarization, hereafter V-pol) microwave data, which were collected at a 54° incidence angle over an 1800 km swath (Long and Hicks 2010). These signals were reconstructed into images in the standardized SIR format as part of the NASA Scatterometer Climate Record Pathfinder project (SCP) (Hicks and Long 2006). We used the egg-based SIR product, which has a nominal enhanced resolution of 4.45 km and an estimated effective resolution of 8–10 km, because

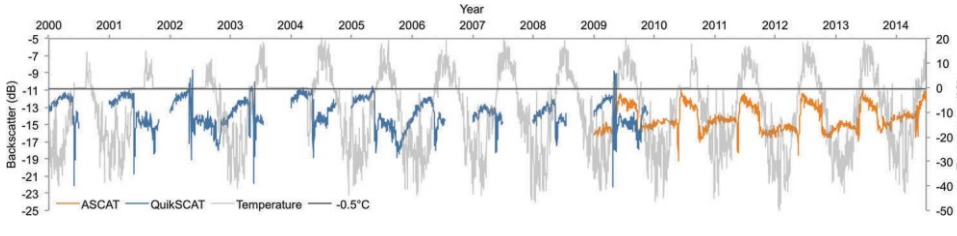

Figure 2. Example time series of scatterometer backscatter and *in situ* air temperature (T_{met}) at Koluktak, 2000–2014 (shown in Figure 1). Daily vertically-polarized (V-pol) time series of QuikSCAT (blue) and ASCAT (orange) backscatter are plotted with *in situ* air temperature (light gray). The horizontal gray line marks −0.5°C, the threshold used in the melt proxy.

it is less sensitive to noise than the higher-resolution slice product (Wang, Derksen, and Brown 2008).

3.1.2. ASCAT

ASCAT C-band (5.255 GHz frequency, 5.7 cm wavelength) backscatter measurements are collected on the MetOp satellite suite at incidence angles between 33° and 62° over a 550 km double swath (Lindsley and Long 2010a). MetOp-A was launched in 2006 and the planned launches of MetOp-B and MetOp-C are designed to ensure ASCAT data continuity beyond 2020. ASCAT measures V-pol C-band backscatter two times per day at polar latitudes. The < 25 km spatial resolution backscatter measurements from the SZF product are normalized to a 40° incidence angle and an adapted SIR algorithm is applied to reconstruct the scatterometer data to the 4.45 km standardized grid (Lindsley and Long 2010a). Unlike QuikSCAT, ASCAT has a coarser temporal resolution and therefore images are two-day reconstructions from four overpasses (Lindsley and Long 2010b). ASCAT SIR products have a lower effective resolution than QuikSCAT products and exhibit greater error variance than QuikSCAT over land (Lindsley and Long 2010b). The enhanced resolution time series utilized in this study began in January 2009, the single year of overlap between ASCAT and QuikSCAT.

3.1.3. Microwave scattering over tundra at Ku- and C-band

Satellite-borne scatterometers emit microwave energy (0.3 to 300 GHz frequencies) and measure the scattering returned from the Earth surface. Backscatter, expressed in dB, measures the ratio of reflected microwave energy to emitted microwave energy. The interactions between emitted microwave energy and snow cover are influenced both by sensor parameters (e.g., frequency, polarization, overpass timing, and viewing geometry) and snowpack parameters (e.g., snow density, liquid water content, snow grain size and shape, stratification, and surface roughness) (Ulaby et al. 1981). Microwave energy is particularly sensitive to texture and moisture, making it suitable for detecting changes in snowpack composition.

Microwave scattering with dry snow occurs at the top of the snow surface, from within the snowpack (volume scattering), and from the ground surface below the snowpack (Scherer et al. 2005). The scattering responds to compositional traits of the snowpack: liquid water content, air-snow interface, snow pack layering, grain size, and grain shape (Nghiem and Tsai 2001; Wagner et al. 2013). Scattering from the frozen ground under the snowpack is more common in a dry snowpack, whereas wet snow causes snow surface scattering and enhances the influence of surface roughness. Rough wet snow generally has a stronger backscatter signal than smooth wet snow, which causes greater specular scattering (Wagner et al. 2013).

The two sensors employed here, QuikSCAT and ASCAT, have different wavelengths, overpass frequencies, and viewing geometries. The differences in sensor parameters affect their sensitivity to snowpack phenomena. In general, the higher frequency of QuikSCAT (13.4 GHz) is responsive to moisture fluctuations in a dry snowpack. This is predicted by Rayleigh approximation and confirmed in the field (Nghiem and Tsai 2001; Ashcraft and Long 2006). In contrast, the lower frequency of ASCAT (5.3 GHz) tends to react more strongly to soil moisture variation than to snowpack moisture (Mortin et al. 2014). An abrupt decrease from winter values is a consistent seasonal melt signal in daily Ku-band backscatter and is followed either by an increase above winter levels in response to an ice

crust or increased daily variability as moisture saturates the snowpack and eventually reveals bare ground (e.g. Figure 2) (Bartsch et al. 2010). Summer Ku-band backscatter over tundra is highly variable, unlike over glaciers, where summer backscatter is consistently higher than winter (Ashcraft and Long 2006; Trusel, Frey, and Das 2012). In contrast to QuikSCAT, there is poor documentation of ASCAT backscatter time series over tundra snowscapes.

ASCAT C-band backscatter time series have a smaller dynamic range, with darker winter and brighter summer signals than Ku-band. These differences limit the options for a consistent algorithm design. In contrast to Ku-band QuikSCAT, C-band scattering from ASCAT is less sensitive to changes in the moisture content of dry snow and reacts more variably to the conditions of melt onset (Ashcraft and Long 2006; Bartsch et al. 2010). Rough snow surfaces, topographic complexity, or summer-like conditions (e.g. bare ground, thin snow, protruding vegetation) within a pixel footprint may neutralize the darkening effect of melt onset on the backscatter signal and cause a weak melt signal (Wagner et al. 2013). Similar to Ku-band, refrozen snow can have bright C-band backscatter signals near summer levels (Bartsch et al. 2010).

3.2 *Ancillary data*

3.2.1. *Surface air temperatures*

To calibrate and validate the backscatter detection of melt onset, we used air temperature, snow depth, and reflected radiance measured at meteorological stations and air temperature modelled by reanalysis. The U.S. Geological Survey Permafrost and Climate Monitoring Network (PCMN) measures *in situ* surface air temperature (T_{met}), snow depth, reflected radiance at 16 sites across the North Slope (Figure 1). Temperature sensors are installed 3 m above the ground and measure T_{met} at 30-second intervals, which are averaged to 1-hour increments (Urban and Clow 2014). Snow depth is measured using the distance to the surface from a stationary pole and confirmed by high-reflected solar-flux values, which are calibrated during the summer. Errors in snow depth measurements may occur during high winds and blowing snow, which are detected and flagged (Urban and Clow 2014). For this study, we used data from 14 sites and aggregated *in situ* hourly data to daily means to mimic the temporal resolution of commonly available temperature data and to facilitate the application of the method to future studies.

The National Centers for Environmental Prediction (NCEP) North American Regional Reanalysis (NARR) estimates daily mean air temperature for 32-km grid cells across North America using the Regional Data Assimilation System (RDAS) and a high-resolution model (Mesinger et al. 2006). NARR data were provided by the NOAA/OAR/ESRL PSD, Boulder, Colorado, USA, from their website at http://www.esrl.noaa.gov/psd/.

3.2.2. *Air temperature as a melt proxy*

Air temperature closely approximates conditions of the dominant causes of melt, such as longwave radiation and the heat regime of the near-surface atmosphere (Ohmura 2001). However, mean surface air temperature is imperfect as a melt proxy because (i) it is aggregated over a 24-hour period which includes low nighttime values; (ii) the phenomenon of melt decreases the temperature of the surrounding air; and (iii) water may not change phase at 0°C owing to the variability of solute concentrations (Colliander et al. 2012). Surface energy balance controls snowmelt (Male and Granger 1981; Marks and Dozier

1992; Zhang, Bowling, and Stamnes 1997; Mioduszewski et al. 2015), but PCMN meteorological stations do not measure the components of the energy balance – radiative fluxes, energy advection, and turbulent heat fluxes. In their absence, we calibrated air temperature melt detection to changes in snow depth. Reanalysis air temperatures at 32 km resolution were used as an independent source of comparison. However, the coarse spatial resolution and reliance on model products renders reanalysis temperatures imprecise in contrast to the backscatter datasets.

In our *in situ* data, an increase in T_{met} toward 0°C consistently corresponds to a decrease in snow depth for all available sites and melt seasons (e.g. Figure 3). We found that pronounced changes in QuikSCAT backscatter during the melt season correspond to increases of mean daily air temperature around 0°C (e.g. Figure 2). These observations are supported by other backscatter melt detection work (Rotschky et al. 2011; Howell et al. 2012; Mortin et al. 2014).

4. Methods

4.1. Overview

We optimized an empirically-based melt detection algorithm for consistency between both QuikSCAT and ASCAT and we confirmed the documented drop in Ku-band and C-band returns at snowmelt by comparing QuikSCAT and ASCAT backscatter time series with melt proxies. First, we developed an algorithm that draws on techniques for detecting melt timing with QuikSCAT backscatter and performed a sensitivity study to optimize algorithm parameters. Next, we applied the algorithm to daily backscatter of each SIR pixel across the Alaskan North Slope from 2000–2014 and validated the resulting melt onset dates via comparison with ancillary data. Last, we compared the performance of the melt onset detection from both datasets in 2009, using point-to-point comparison of the melt onset maps and comparison of the accuracy results against a temperature melt proxy.

4.2. Melt onset detection with backscatter

The proposed algorithm detects seasonal melt onset using a departure threshold from running median with a temporal filter. The algorithm was initially developed through rigorous iteration in which backscatter time series were plotted with *in situ* air temperature, snow depth, and reflected radiance data (e.g. Figure 3) and the parameters were selected through empirical comparisons with air temperature melt proxies. The method was based on terrestrial melt detection from QuikSCAT that employed a 1.7 dB departure threshold from a 5-day running mean with a 3-day persistence criterion to detect melt onset (Wang, Derksen, and Brown 2008; Wang et al. 2009).

Melt was detected for each pixel from time series of daily backscatter using a departure threshold from the running median. Melt events were detected when:

$$M_i = 1; if\ sigma0_i < median(sigma0_{i-15} : sigma0_{i-1}) - t \quad (1)$$

where M_i is the melt index for day i (a value of 1 indicates a melt event), $sigma0_i$ is the backscatter for day i, and t is the threshold value in dB. The algorithm detected a melt event when daily backscatter deviates below the dynamic baseline by more than the threshold value. The baseline value was calculated as a 14-day running median, which was optimized to represent dry snow conditions at the study pixel from the two weeks

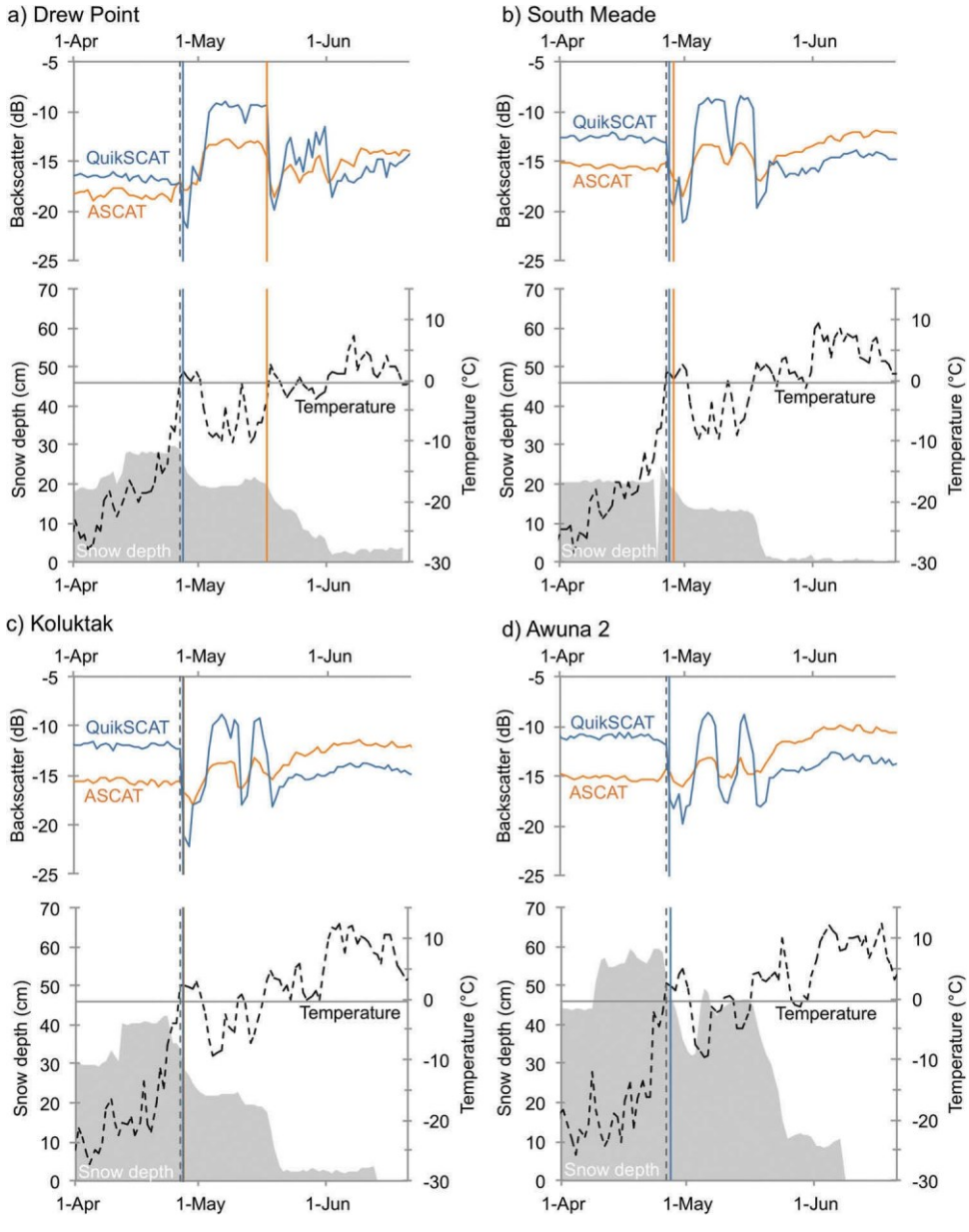

Figure 3. Time series of scatterometer and *in situ* data at meteorological station sites during the 2009 melt season (1 April – 20 June). Sites are ordered by distance from coast (refer to Figure 1): a) Drew Point, b) South Meade, c) Koluktak, and d) Awuna 2. Daily time series of vertically polarized sent and received (V-pol) QuikSCAT (blue line) and ASCAT (orange line) are plotted above *in situ* snow depth (solid gray) and air temperature (T_{met}) (dashed black line). Vertical lines indicate melt onset dates detected by QuikSCAT (blue), ASCAT (orange), and T_{met} (dashed).

immediately preceding the day under evaluation. We additionally defined the timing of *melt onset* as the commencement of the melt season for each year, and identified it as the first occurrence of 2 melt events in a 3-day period. Persistence criteria are commonly used to filter out potential erratic melt events that are followed by a return to frozen-state

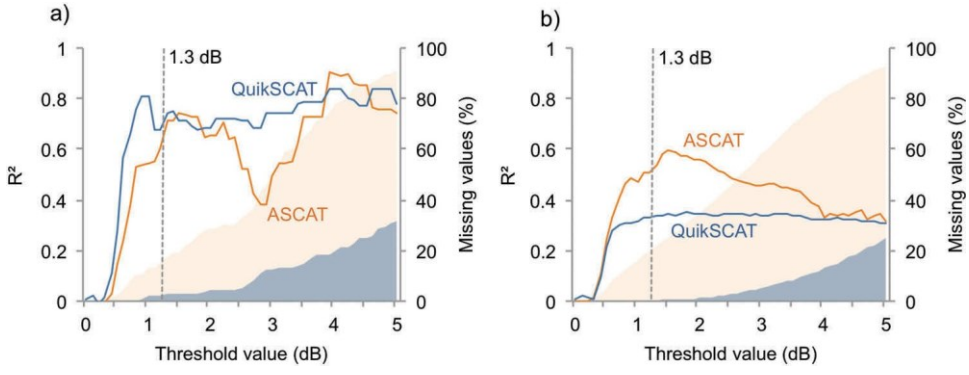

Figure 4. Sensitivity of backscatter melt onset algorithms to melt onset detected by a) *in situ* temperatures (T_{met}) at the 14 meteorological stations and b) NCEP NARR reanalysis 2-m air temperature (T_{2m}). Algorithms were applied to QuikSCAT backscatter 2000–2009 (blue) and ASCAT backscatter 2009–2014 (orange) with thresholds ranging from 0 to 5 dB in intervals of 0.1 dB. Daily mean temperatures greater than −0.5°C were considered a proxy for melt. Solid lines show goodness of fit (R^2) of detected onset dates and shaded areas show percentage of scatterometer pixels where the algorithm failed to detect melt onset. Goodness of fit was calculated from ordinary least squares linear regression between scatterometer-detected onset dates and temperature-detected dates. Vertical lines mark 1.3 dB, the threshold value that optimized the melt-detection algorithm (see Section 4.2).

conditions and may require 2 to 5 days of persistent melt signal (e.g. Brown, Derksen, and Wang 2007; Wang, Derksen, and Brown 2008; Howell et al. 2012).

We evaluated the sensitivity of melt onset detection to backscatter departure threshold values ranging from 0–5 dB in increments of 0.1 dB. To do so, we quantified the agreement using linear regression between melt onset dates detected from backscatter and those detected from temperature as described below (Figure 4). We summarized the results for each threshold value with the coefficient of determination (R^2) and the percentage of pixels with unsuccessful melt detection. The backscatter change threshold that optimizes the melt-detection algorithm is 1.3 dB, which we arrived at through the following process. ASCAT has a weaker melt signal so we optimized the threshold first for ASCAT by identifying all thresholds that satisfy the criteria of $R^2 > 0.5$ and missing values < 25% for ASCAT. Next, we found the QuikSCAT value that produced the strongest correlation with ASCAT values for the single year of overlap (2009). As threshold values increase, there is a steep increase in ASCAT missing values (Figure 4). QuikSCAT appears less sensitive to the change in threshold values. We performed numerous spot checks to compare backscatter time series to *in situ* data (e.g. Figure 3). We observed good performance with these parameters. Using the optimized parameters, we then produced annual maps of the date of melt onset across the North Slope for each year by applying the melt detection algorithm to annual time series of QuikSCAT backscatter from 2000–2009 and ASCAT backscatter from 2009–2014.

4.3. *Validation with temperature*

Scatterometer-derived melt onset dates were validated against temperature-derived onset dates using ordinary least squares linear regression, based on the assumption that daily mean temperature can approximate melt onset. To address the limitations of

this assumption, discussed above, we tested the sensitivity of temperature threshold and persistence criteria to melt detection with backscatter. The threshold of −0.5°C optimized the sensitivity of the melt proxy given that melt can occur when mean temperatures remain below 0°C. For consistency with the scatterometer melt detection, we defined temperature melt onset as the first occurrence of 2 days of melt within a 3-day period.

To compare scatterometer data to T_{met}, we used the SIR pixel whose spatial footprint includes the meteorological station. To compare scatterometer data to T_{2m}, we resampled the 4.45-km gridded onset DOY data to the 32-km NARR grids using the median DOY of all pixels within the NARR grid. We compared the correlation coefficients and adjusted R^2 values between pairs of melt onset datasets (Figure 5).

4.4. *Comparison of melt detection between sensors*

To assess the ability of ASCAT to extend the QuikSCAT melt onset record, we compared both the temperature validation described above and the melt onset images from both scatterometer sensors for 2009, the only year of overlap between the two datasets. We conducted a point-to-point comparison between 2009 ASCAT dates and 2009 QuikSCAT dates and further compared these areas to the T_{2m} dates. Pixels with greater than three days of difference in detected onset dates were masked from further analysis. This conservative masking approach ensured that melt onset time series were consistent across decades.

5. Results

5.1. *Backscatter signatures of melt onset*

Melt signals are visible in annual time series of backscatter from both QuikSCAT and ASCAT over the tundra of the North Slope (e.g. Figures 2 and 3). Time series from both sensors display clear differences between dry snow and melting snow conditions, as both exhibit increasing backscatter during the winter caused by the changes in scattering as dry snow covers frozen ground (Ulaby and Stiles 1980). However, melt signals differ between the two sensors. Ku-band from QuikSCAT (V-pol, one-day reconstruction) backscatter values drop at the first appearance of moisture in the snowpack, fluctuate during the melt season and summer, stabilize at low values in response to frozen ground, and gradually increase throughout the winter (e.g. Figure 2). We observe that the summer signal in C-band from ASCAT (V-pol, two-day reconstruction) is brighter and less variable than in Ku-band, whereas ASCAT exhibits darker dry snow values than QuikSCAT. ASCAT winter backscatter values tend to drop at melt and then increase in steps to brighter summer values. As a result of these differences, unlike QuikSCAT backscatter, which may require only a static threshold, ASCAT backscatter requires a dynamic and customized algorithm to distinguish between dry snow and melting conditions. Despite these differences, a departure threshold of 1.3 dB is able to detect melt events in both QuikSCAT and ASCAT time series.

5.2. *Accuracy of melt onset dates*

Comparisons between temperature melt proxies and backscatter melt detection are provided in scatterplots (Figure 5). The greatest overall disagreement is exhibited between

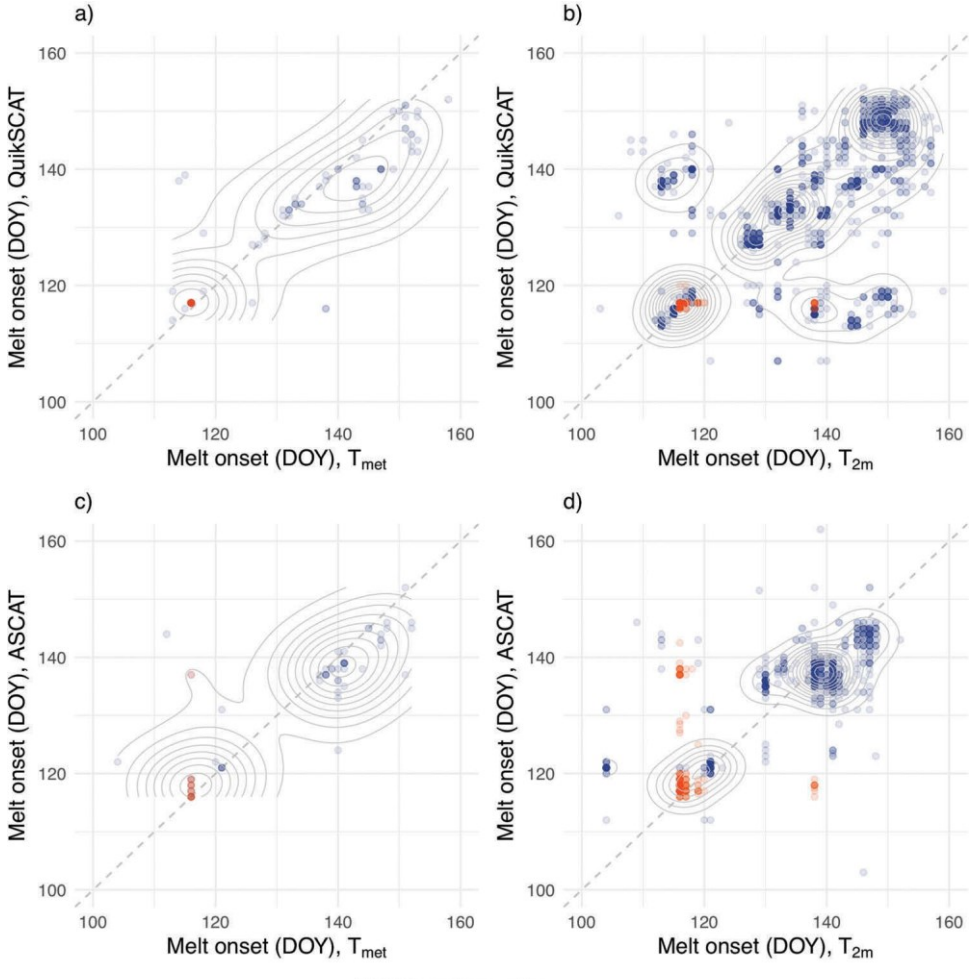

OLS Linear Regression

	Slope	Intercept	R^2	P-value	N	RMSE	MD	MAD
QuikSCAT vs. T_{met}	0.71	37.77	0.75	<0.001	82	5.51	-1.82	4.12
QuikSCAT vs. T_{2m}	0.55	58.54	0.35	<0.001	1700	9.83	-2.7	7.07
ASCAT vs. T_{met}	0.67	44.02	0.72	<0.001	58	5.51	0.13	3.64
ASCAT vs. T_{2m}	0.63	48.95	0.63	<0.001	1011	5.64	0.3	4.24

Figure 5. Plots of melt onset timing detected by the backscatter algorithm versus detected from air temperature for all available point-to-point comparisons 2000–2014. Point density is represented using point transparency (alpha = 0.15) and contour lines. Density contour lines used a Gaussian kernel density estimator with bandwidth based on a normal reference distribution. The dashed line is the 1:1 line. Orange points indicate dates from 2009, the QuikSCAT and ASCAT overlap period. Top plots compare QuikSCAT with a) *in situ* temperatures (T_{met}) and b) modelled 2-m air temperature (T_{2m}) and bottom plots compare ASCAT with c) T_{met} and d) T_{2m}. To compare scatterometer data to T_{2m}, the 4.45-km SIR grids were resampled to the 32-km NARR grids using the median value of all pixels within the NARR gridcell. Summary values of the ordinary least squares (OLS) linear regression, Root Mean Squared Error (RMSE), Mean Deviation (MD), and Mean Absolute Deviation (MAD) are presented in the associated table.

QuikSCAT and T_{2m}, with a mean absolute deviation (MAD) of about 7 days and mean deviation (MD) of about −3 days. The agreements between backscatter and temperature in the other three comparisons all have MAD of approximately 4 days. The coefficients of the OLS linear regressions suggest that the backscatter algorithm is less sensitive to early-season melt than the temperature melt proxies (Figure 5). However, as noted previously, temperature is a proxy that indicates when surface air temperature is conducive to melt whereas backscatter detects the presence of moisture. The date detected by backscatter may be more accurate. For example, in the low-elevation foothills T_{2m} detected melt onset on DOY 104 and ASCAT, supported by T_{met}, detected melt on DOY 122 (Figure 5d).

5.3. *Detected melt onset*

5.3.1. *QuikSCAT*

QuikSCAT and temperature melt onset dates deviated with root mean square error (RMSE) of 5.5 days for *in situ* and 9.8 days for reanalysis (Figure 5). Melt onset detected from QuikSCAT across our study area for the years 2000–2009 occurred around a median timing of DOY 134 with an interquartile range of 119–143 (Figure 6). We observe three patterns of melt onset: near-simultaneous melt onset in early or mid May (2002, 2004, and 2006); gradual melt onset that progresses from southwest to northeast in mid to late May (2000, 2001, and 2007); and dichotomous onset that occurred first in the foothills in late April and a month later on the coastal plain (2003, 2005, and 2008; Figure 6).

5.3.2. *ASCAT*

On average, ASCAT failed to detect melt onset in 24% of the pixels in the study area each year. In multiple years, ASCAT missed melt detection in patches of high-elevation foothills, most commonly in western zones (Figure 7). Other areas of missed detection were more anomalous, such as a large area south of Point Barrow where melt was not detected in 2013.

Of the pixels where ASCAT did detect melt onset for 2009–2014, ASCAT and temperature melt onset dates deviated (RMSE) by 5.5 days for *in situ* and 5.6 days for reanalysis (Figure 5). The ASCAT-derived time series of melt onset dates exhibited low interannual variability in contrast to the 2000–2009 time series. Melt onset events in the ASCAT-derived time series occurred around a median timing of DOY 136 (mean 133) with an interquartile range of 121–139 (Figure 7). We observe two patterns of melt onset: near-simultaneous melt onset in late April (2009 and 2014) and gradual progression of melt onset from south to north (2010–2013). These melt onset patterns match the categories identified in the QuikSCAT-derived dataset. However, the ASCAT results tend to exhibit more patchiness.

5.4. *Inter-sensor comparison*

Overall, ASCAT detected melt onset more conservatively than QuikSCAT. Across all years, ASCAT was unable to detect melt onset in 24% of the evaluated pixels whereas QuikSCAT missed detection in 0.5%. However, ASCAT exhibited better agreement than QuikSCAT with T_{2m} (Figure 5).

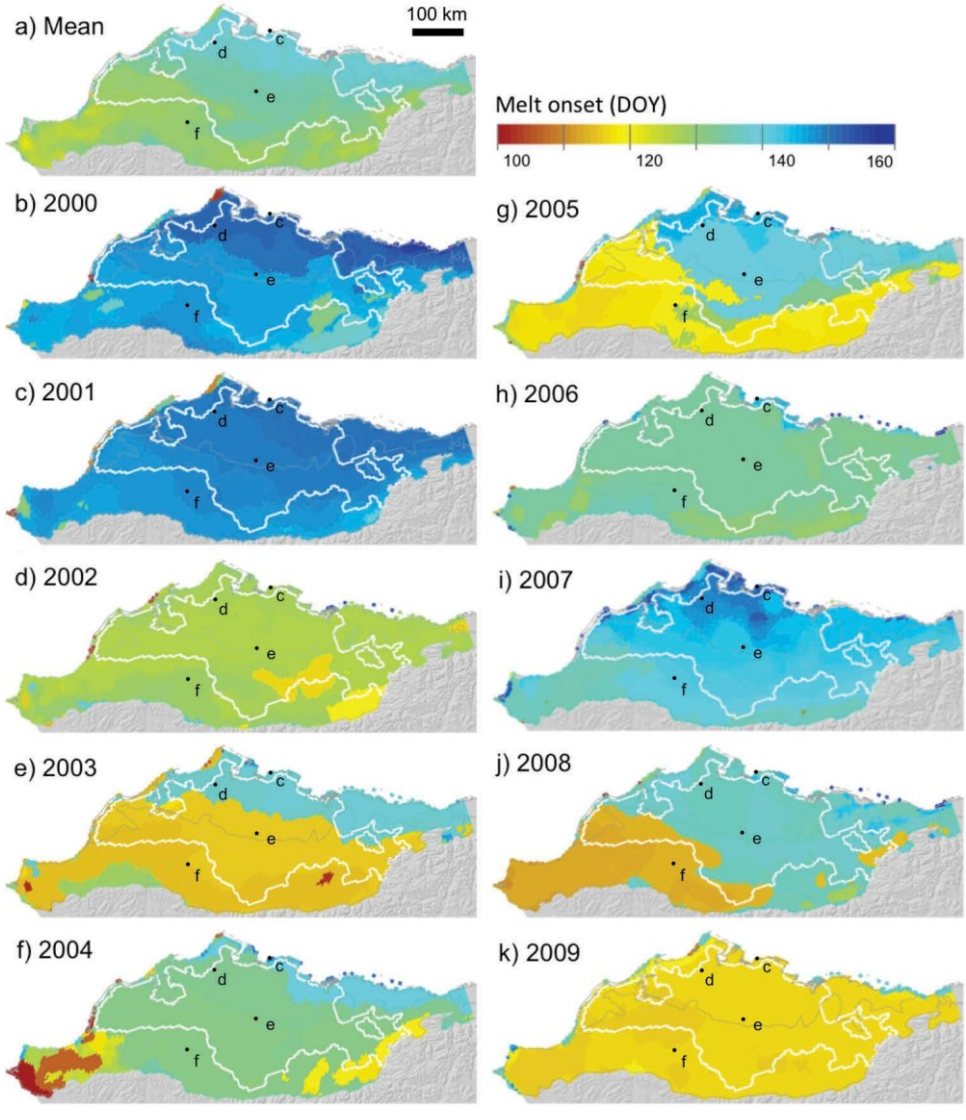

Figure 6. Day of year (DOY) of melt onset detected from QuikSCAT V-pol daily backscatter: the 2000–2009 mean (a) and the melt maps from 2000 (b), 2001 (c), 2002 (d), 2003 (e), 2004 (f), 2005 (g), 2006 (h), 2007 (i), 2008 (j), and 2009 (k). The white line outlines the area with consistent results (< 4 days of difference) between the two datasets. The gray line represents the boundary between the ecoregions (Brooks Foothills and Beaufort Coastal Plain). Example PCMN stations are indicated for references (black points, see Figure 1).

Direct comparison of melt onset timings derived from each sensor was limited to 2009, the only melt season for which the SIR image time series overlapped. We considered the melt onset datasets in agreement when the dates detected by ASCAT were equal to QuikSCAT dates ± 3 days. Regions with > 3 days of difference in detected onset dates were masked from further analysis to ensure consistency of melt onset time series and to account for the potential error introduced by the 3-day persistence filter (Figure 8).

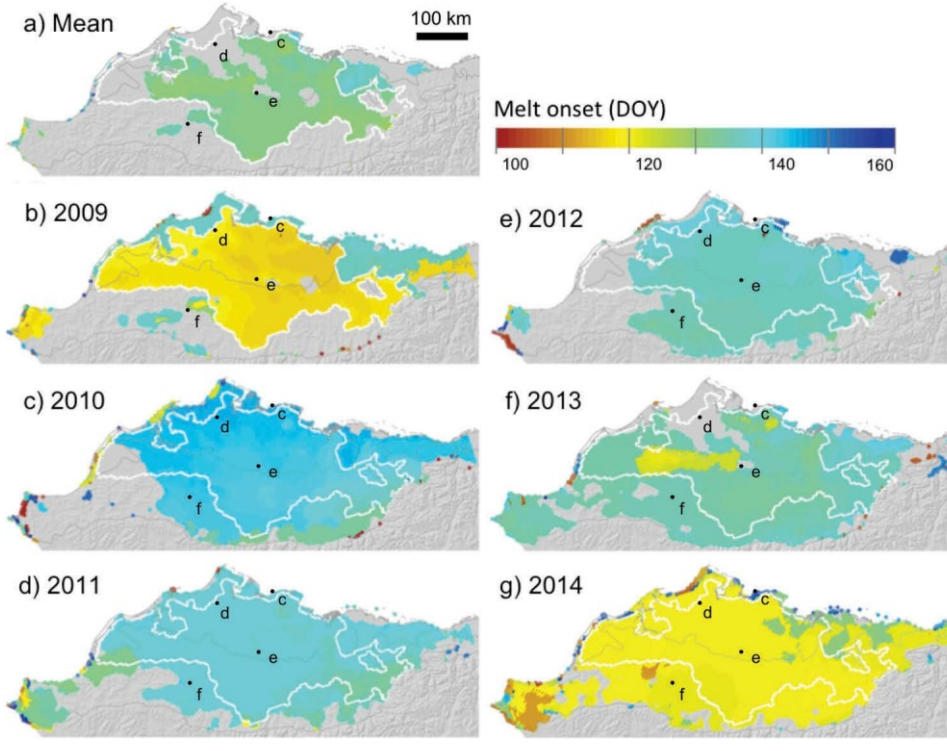

Figure 7. Day of year (DOY) of melt onset detected from ASCAT V-pol daily backscatter: the 2009–2014 mean (a) and melt maps for 2009 (b), 2010 (c), 2011 (d), 2012 (e), 2013 (f), and 2014 (g). The white line outlines the area with consistent results between the two datasets. The gray line represents the boundary between the ecoregions (Brooks Foothills and Beaufort Coastal Plain). Example PCMN stations are indicated for references (black points, see Figure 1).

In the 2009 dataset produced from ASCAT, melt onset timings were not detected in 32% of the study area and disagreed with QuikSCAT-derived timings in 16% of study area (Figure 8). The median difference where melt onset timings disagreed was 20 days with small dispersion (3 day interquartile range). These differences occurred where ASCAT failed to detect the first early-season melt event and instead characterized a later event as melt onset (Figure 9). That later event occurred in mid May (median DOY 137), 20 days later than the melt onset detected by QuikSCAT. These areas of disagreement in 2009 occur primarily along the coast with two patches in the foothills as well.

Of the pixels where both datasets detected melt onset, dates agreed at 76% of pixels (+/- 3 days). ASCAT-derived dates exhibited greater dispersion than those detected by QuikSCAT, which registered melt onset for almost the entire region on 26–27 April (DOY 116–117). In contrast to the near-uniform detection of melt onset across the entire North Slope by QuikSCAT for 2009, ASCAT measured melt onset over a 5-day period of 26–30 April (DOY 116–120) in the low-elevation coastal plain. In the ASCAT dataset, melt onset appears to progress from east to west during the 5-day event (Figures 7 and 8).

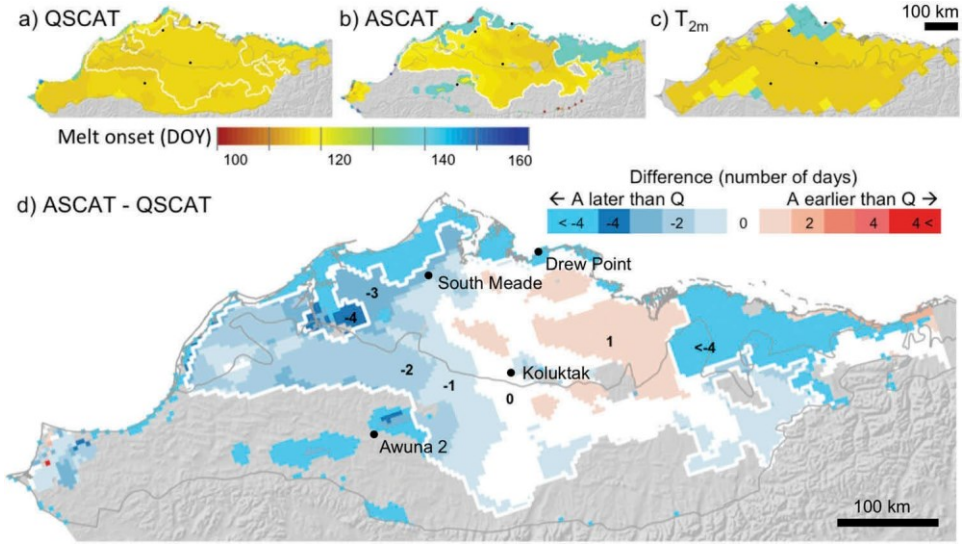

Figure 8. Day of year (DOY) of melt onset in 2009 derived from a) QuikSCAT (Q; QSCAT) V-pol daily backscatter, b) ASCAT (A) V-pol daily backscatter, and c) reanalysis 2-m air temperatures. d) Difference between QuikSCAT and ASCAT detected melt onset. Blue areas are where ASCAT detected melt later than QuikSCAT and red are the inverse. The white line outlines the area with consistent results between the two datasets. The gray line represents the boundary between the ecoregions (Brooks Foothills and Beaufort Coastal Plain). Example PCMN stations are indicated for references (black points, see Figure 1).

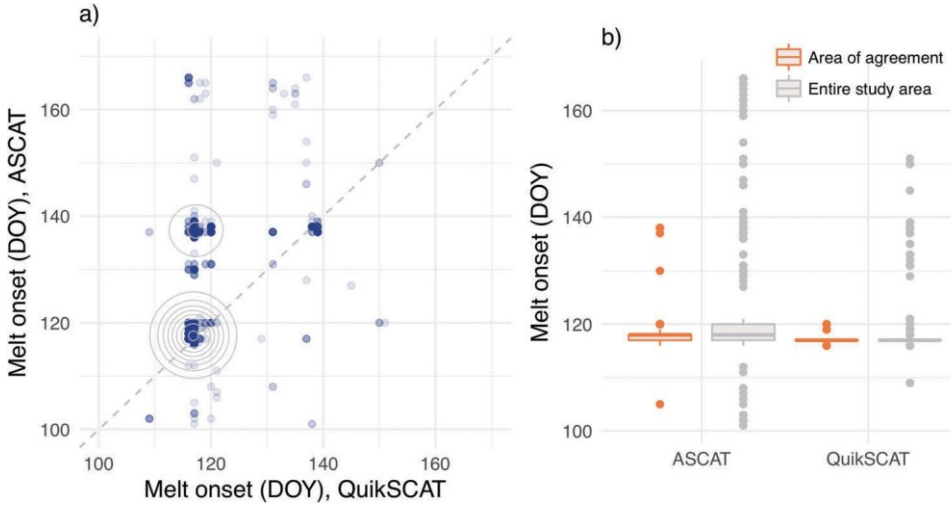

Figure 9. a) Scatterplot of melt onset in 2009 at each pixel detected by QuikSCAT (x-axis) and ASCAT (y-axis); and b) the distribution of 2009 melt onset values detected by QuikSCAT and ASCAT only from the area of agreement, where there were fewer than 4 days of difference in onset detected by each dataset (orange, n = 4,105) and in the entire study area (gray, n = 5,798).

5.5. Melt onset patterns

Over the 15-year multi-sensor time series, melt onset occurred on average on 12 May (mean DOY 133; median DOY 135) (Figure 10) with an interquartile range spanning 1–20 May (DOY 122–141). Overall, melt onset consistently occurred first in the southwest around Point Hope and last in the northeast along the Beaufort Sea coast near Drew Point. This pattern was stronger in the QuikSCAT portion of the time series. The year with the earliest median melt onset was 2009 (Figure 6k), when melt onset occurred across the entire study area on 26–27 April (DOY 116–117). The earliest 25th percentile date for any year was also 26 April (DOY 116) in 2003 in the low Foothills. The latest 75th percentile date for any year occurred in 2000 when the northeastern coast experienced melt onset on 30 May (DOY 151).

Melt onset events can be classified as early (late April to early May) or late (mid to late May) season. The most typical melt onset takes place in mid to late May (DOY 130–153). This type of melt onset progression is gradual and can occur over 5–15 days, as in 2007 and 2011, respectively. It tends to progress from the Point Hope region toward the north and east; the Beaufort Sea Coast tends to experience melt last, as described above. This is a similar pattern exhibited in surface air temperatures (T_{met} and T_{2m}) in years with typical melt onset, which indicate gradual warming of the North Slope from south to north and from west to east, likely driven by seasonal increases in solar elevation and the advection of warm Pacific waters toward the perennial sea ice pack in the Chukchi and Beaufort Seas (Wendler, Shulski, and Moore 2010; Kittel et al. 2011).

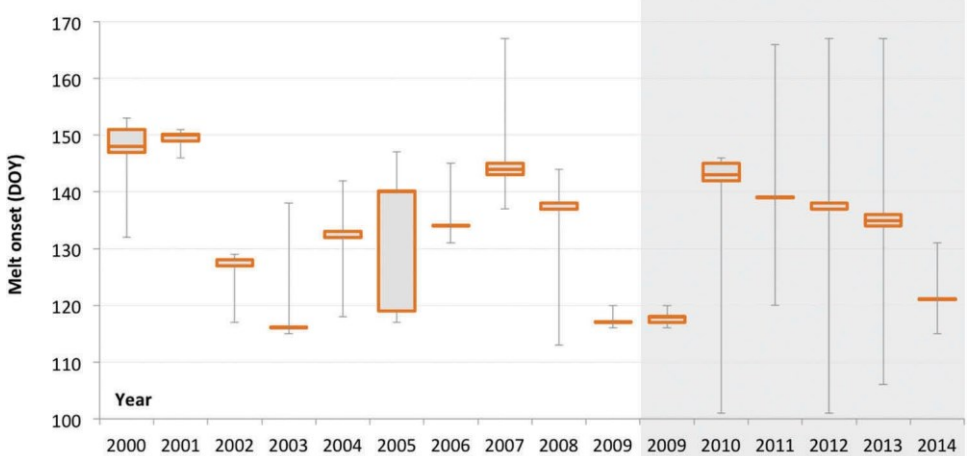

Figure 10. Annual distributions of melt onset timing in the area of agreement from QuikSCAT and ASCAT (n = 4,105). Results are only presented for the area of agreement between sensors in 2009 (see Sections 4.4 and 5.4). In 2005, the median DOY and the 75th percentile are equal so the median line is not visible. The box plot of 2009 in QuikSCAT is a single line indicating minimal variation from the median of DOY 117.

In contrast, early season melt onset events typically affect a wide areal expanse over only one or two days and occur during late April or early May (before DOY 125). These events may affect the whole study area, as in 2009 and 2014, or leave some isolated areas with a more typical pattern of late season melt, such as in 2003 and 2008. Early season melt onset appears to be related to passing weather systems that cause rapid heat advection from the Pacific Ocean in the south through the Bering Strait and across the North Slope (Stone et al. 2002). This early melt onset provides insight for the role of atmospheric circulation in the seasonality of the region.

The reduced variability in the 2009 and 2014 melt onset across the region is likely due to warm weather events triggering early melt onset over the entire North Slope, whereas years with later (more typical) melt onset have a gradual melting pattern. The lack of spatial variability with early season melt events suggests the occurrence of sudden warming events caused by southerly advection (Wendler, Shulski, and Moore 2010). The frequency of early melt onset is expected to increase in accordance with increasing frequency of spring cyclones on the North Slope (Wendler, Shulski, and Moore 2010)

6. Discussion and conclusions

In this study, we show that QuikSCAT and ASCAT radar scatterometer backscatter datasets enable detailed time series mapping of the timing of melt onset over tundra areas in the Arctic. Using the detection algorithm developed in this study, the 10-year time series of melt onset derived from QuikSCAT backscatter (2000–2009) was extended to 15 years across the Alaskan North Slope by deriving melt onset from ASCAT data (2009–2014). The timing of melt onset can be determined to 3 days with a spatial resolution of 4.45 km x 4.45 km. In addition to being more spatially precise than reanalysis climate variables, melt onset is empirically measured rather than modelled. There is the potential for robust observations of shifts in the timing of melt onset that will become more rigorous as longer scatterometer time series are collected. Using the 1.3 dB departure threshold from a running 14-day median, ASCAT and QuikSCAT backscatter time series indicate melt with 76% agreement (± 3 days) in the BCP study area and low-elevation Foothills. They correlate with *in situ* temperature with linear trends similar to 1:1 and coefficients of determination of ~0.75 (QuikSCAT) and ~0.72 (ASCAT).

The overlap period of the two SIR datasets limited our analysis to a single year with an anomalous melt pattern. The year 2009 exhibited anomalously early melt onset in the QuikSCAT dataset, which was detected by ASCAT for half of the area. As such, the 2009 melt season provides an incomplete understanding of the differences between the ASCAT and QuikSCAT backscatter signals. While interpretations of the results must acknowledge this limitation, we are able to draw conclusions about the tundra snowmelt signals in the two datasets and ultimately, to produce a consistent record of melt onset.

Our results indicate important differences between the sensitivities of the sensors to such variables as topography, snowpack, and meteorology. Melt detection is more spatially limited and more conservative when performed with ASCAT data than with QuikSCAT. ASCAT melt onset results have more missing values, which predominantly occur in higher elevations where topographic complexity is greater than on the coastal plain. Melt onset dates detected in those topographically complex areas may be less accurate than QuikSCAT results. Agreement between the sensors is better on the BCP where the same weather patterns affect broad regions and where melt onset dates detected by both sensors are consistent with *in situ* and modelled air temperature.

Ku-band and C-band backscatter measured by the two sensors have similar responses to moisture content in dry snow. Consistent with observations of backscatter over sea ice (Mortin et al. 2014), ASCAT is more sensitive than QuikSCAT to non-melt signals, such as those from land surface texture and properties within the snowpack. As a result, it is less sensitive to early season melt onset particularly in areas with topographic complexity.

Despite the differences between the two scatterometer datasets, they exhibit convergent central tendencies and similar relationships to the temperature melt proxy. These convergent relationships enable consistent monitoring of melt onset at the regional scale.

The algorithm executed for subsequent years on the North Slope will generate an increasingly robust time series. Furthermore, this method to detect tundra melt onset beyond the temporal extent of the QuikSCAT time series can be applied at other tundra regions with site-specific calibration.

The ability to determine the timing of seasonal melt onset across the Alaskan North Slope is important for enhanced understanding of climate patterns and associated climate feedbacks. The 15-year time series presented here is too short and variable to permit a robust analysis of trends, but the collection of melt onset maps suggests the relationship of melt onset timings to ongoing climate change across the region. The North Slope melt regime is driven by solar irradiance, atmospheric and oceanic circulation, and regional feedbacks (Shulski and Wendler 2007; Arp and Jones 2009; Kittel et al. 2011). The effects of the temperature gradient caused by pressure zones and associated winds are visible in the overall melt onset pattern. They indicate the gradual seasonal weakening of the atmospheric ridge that maintains stable low temperatures in the Arctic Basin during the winter (Francis and Vavrus 2012). Typical (late-season) melt onset events are indicative of stable atmospheric circulation patterns in which melt progresses gradually from the south to the north and the west to the east, along gradients of latitude and distance from the southern Chukchi Sea, a source of heat advection to the isolated North Slope (Wendler, Shulski, and Moore 2010). In contrast, early season, more instantaneous melt onset events suggest that a weather event was strong enough to either force southern warm air over and around the Brooks Range and/or mix out the winter inversion to bring warm air to the surface. In these cases, a strong Aleutian Low is associated with increased cyclonic activity on the North Slope (Kittel et al. 2011).

Studies have identified greater frequency of extratropical cyclones in high latitudes of North America in recent decades, although there is low confidence in trends of storminess and projections of changing wind patterns remain inconclusive (IPCC 2014). Ongoing analysis of melt onset time series such as those presented in this study may offer an additional proxy measure of storminess, given that early-season melt events are consistently caused by extreme weather events, such as extratropical cyclones.

The timing of snowmelt is integral to snow–albedo and ice–ocean–atmosphere feedbacks (Eugster et al. 2000; Kittel et al. 2011; Zhou et al. 2014). As an example of the ice-ocean-atmosphere feedback, wind patterns that we infer from the melt onset timings also affect sea ice distribution in the Beaufort Sea (Wendler, Shulski, and Moore 2010), which in turn influence atmospheric circulation and land surface melt (e.g. Tang, Zhang, and Francis 2014). By extending the record of snowmelt onset, we improve the ability to monitor such interactions and ongoing change in a vulnerable area.

The different sensitivities of the backscatter data to surface roughness and moisture characteristics present a challenge to creating an extended record. The use of the 2009 overlap period enabled comparison, but this could be strengthened with the robust evaluation of the specific reactions of backscatter measurements from the ASCAT SIR product to snowpack conditions, which was beyond the scope of the current work. In

particular, the sensitivity of ASCAT to soil moisture suggests the potential for detecting freeze-up. Despite these limitations, we present an effective method to extend snowmelt onset detection from QuikSCAT backscatter to ASCAT in snow-covered tundra.

We acknowledge the imprecision of using surface air temperature to approximate melt. Air temperature is only one term in the surface energy balance, and is a less reliable predictor of melt. Additionally, the spatial resolution of the temperature datasets limits comparison. The calibrations of the backscatter signals could be improved at a study area where energy balance or melt data are collected. Despite these limitations, we observed a convergent relationship between timing of snow depth decrease and increase in mean daily air temperature to around 0°C. This agrees with work by Raleigh et al. (2013), who found that air temperatures are correlated with snow surface temperatures with a site-specific positive bias. Our empirical comparisons negate the need to apply a bias, following other melt detection that relied on *in situ* temperature data (Rotschky et al. 2011; Howell et al. 2012; Mortin et al. 2014).

This study presents a spatially continuous 15-year satellite-based time series of melt onset across the Alaskan North Slope that is both more spatially and temporally precise than any other currently available dataset. The extension of the algorithm from QuikSCAT to ASCAT radar backscatter enables ongoing production of a consistent melt onset time series that in turn could be extended to pan-Arctic tundra. The data presented here for the Alaskan North Slope will facilitate ongoing quantifications of the interactions between climate and snowpack phenology. Future trend analyses will become increasingly robust as we continue to detect melt onset from the ASCAT record and lengthen the time series. We hope that the satellite-based methods presented here can be utilized as a proxy for melt onset detection in future analyses of changing atmospheric circulation and climate warming in remote Arctic regions that lack densely spaced meteorological stations.

Acknowledgements

This research was supported by funding from NSF grants AON-1107596 and ARC-1044560 to K. Frey. The dataset of 2000–2014 melt onset across the Alaskan North Slope will be distributed through the National Science Foundation (NSF) Arctic Data Center, part of the Arctic Observing Network (AON) Program (https://arcticdata.io/). We thank Dr. Yongwei Sheng of UCLA for reviewing and improving upon a draft manuscript. We thank the two anonymous journal reviewers whose suggestions improved the work. Any use of trade, firm, or product names is for descriptive purposes only and does not imply endorsement by the authors or the U.S. Government.

Disclosure statement

No potential conflict of interest was reported by the authors.

Funding

This work was supported by the National Science Foundation [ARC-1044560];National Science Foundation [AON-1107596];

ORCID

Emily J. Sturdivant http://orcid.org/0000-0002-2420-3115

References

Arp, C. D., and B. M. Jones. 2009. "Geography of Alaska Lake Districts : Identification, Description, and Analysis of Lake-Rich Regions of a Diverse and Dynamic State." *U.S. Geological Survey Scientific Investigations Report 2008–5215*, 40.

Ashcraft, I. S., and D. G. Long. 2006. "Comparison of Methods for Melt Detection over Greenland Using Active and Passive Microwave Measurements." *International Journal of Remote Sensing* 27 (12): 2469–2488. doi:10.1080/01431160500534465.

Bartsch, A., W. Wagner, and V. Naeimi. 2010. "The Legacy of 10 Years QuikScat Land Applications-Possibilities and Limitations for a Continuation with Metop ASCAT." In *Proceedings of the ESA Living Planet Symposium, Bergen, Norway*. ESTEC, Noordwijk, 1–6.

Brown, R. D., C. Derksen, and L. Wang. 2007. "Assessment of Spring Snow Cover Duration Variability over Northern Canada from Satellite Datasets." *Remote Sensing of Environment* 111 (2–3): 367–381. doi:10.1016/j.rse.2006.09.035.

Callaghan, T. V., M. Johansson, R. D. Brown, P. Y. Groisman, N. Labba, V. Radionov, R. G. Barry, et al. 2011. "The Changing Face of Arctic Snow Cover: A Synthesis of Observed and Projected Changes." *Ambio* 40 (SUPPL. 1): 17–31. doi:10.1007/s13280-011-0212-y.

Colliander, A., K. C. McDonald, R. Zimmermann, R. Schroeder, J. S. Kimball, and E. G. Njoku. 2012. "Application of QuikSCAT Backscatter to SMAP Validation Planning: Freeze/Thaw State over ALECTRA Sites in Alaska from 2000 to 2007." *Geoscience and Remote Sensing, IEEE Transactions On* 50 (2): 461–468. doi:10.1109/TGRS.2011.2174368.

Déry, S. J., and R. D. Brown. 2007. "Recent Northern Hemisphere Snow Cover Extent Trends and Implications for the Snow-Albedo Feedback." *Geophysical Research Letters* 34 (22): 2–7. doi:10.1029/2007GL031474.

Eugster, W., W. R. Rouse, R. A. Pielke, J. P. Mcfadden, D. D. Baldocchi, T. G. F. Kittel, F. Stuart Chapin, et al. 2000. "Land-Atmosphere Energy Exchange in Arctic Tundra and Boreal Forest: Available Data and Feedbacks to Climate." *Global Change Biology* 6 (SUPPLEMENT 1): 84–115. doi:10.1046/j.1365-2486.2000.06015.x.

Francis, J. A., and S. J. Vavrus. 2012. "Evidence Linking Arctic Amplification to Extreme Weather in Mid-Latitudes." *Geophysical Research Letters* 39 (February): 1–6. doi:10.1029/2012GL051000.

Hicks, B. R., and D. G. Long. 2006. "Diurnal Melt Detection on Arctic Sea Ice Using Tandem QuikSCAT and SeaWinds Data." *Proceedings of the IEEE International Geoscience and Remote Sensing Symposium* 4112–4114. doi:10.1109/IGARSS.2006.1054.

Howell, S. E. L., J. Assini, K. L. Young, A. Abnizova, and C. Derksen. 2012. "Snowmelt Variability in Polar Bear Pass, Nunavut, Canada, from QuikSCAT: 2000–2009." *Hydrological Processes* 26 (23): 3477–3488. doi:10.1002/hyp.8365.

IPCC. 2014. "*Climate Change 2014: Synthesis Report. Contribution of Working Groups I, II and III to the Fifth Assessment Report of the Intergovernmental Panel on Climate Change*." Geneva, Switzerland. https://www.ipcc.ch/report/ar5/syr/.

Jones, B. M., and G. Grosse. 2012. *Western Arctic Coastal Plain, IfSAR DSM-Derived Coastline and Coastal Features - Version 2*. University of Alaska, Alaska: Geophysical Institute Permafrost Laboratory.

Kittel, T. G. F., B. B. Baker, J. V. Higgins, and J. Christopher Haney. 2011. "Climate Vulnerability of Ecosystems and Landscapes on Alaska's North Slope." *Regional Environmental Change* 11 (SUPPL. 1): 249–264. doi:10.1007/s10113-010-0180-y.

Lindsley, R. D., and D. G. Long. 2010a. "Standard BYU ASCAT Land/Ice Image Products." *Microwave Earth Remote Sensing Laboratory*, 3 Jun 2010.

Lindsley, R. D., and D. G. Long. 2010b. *Adapting the SIR Algorithm to ASCAT. Geoscience and Remote Sensing Symposium (IGARSS), 2010 IEEE International*. Vol. 84602 vols. Provo, UT: IEEE. doi:10.1109/IGARSS.2010.5650207.

Long, D. G., and B. R. Hicks. 2010. "*Standard BYU QuikScat and SeaWinds Land/Ice Image Products. Brigham Young Univ., Provo, UT, QuikScat Image Product Documentation*." Provo, UT. http://www.scp.byu.edu/docs/pdf/QscatReport6.pdf.

Male, D. H., and R. J. Granger. 1981. "Snow Surface Energy Exchange." *Water Resources Research* 17 (3): 609–627. doi:10.1029/WR017i003p00609.

Marks, D., and J. Dozier. 1992. "Climate and Energy Exchange at the Snow Surface in the Alpine Region of the Sierra Nevada: 2. Snow Cover Energy Balance." *Water Resources Research* 28 (11): 3043–3054. doi:10.1029/92WR01483.

Mesinger, F., G. DiMego, E. Kalnay, K. Mitchell, P. C. Shafran, W. Ebisuzaki, D. Jović, et al. 2006. "North American Regional Reanalysis." *Bulletin of the American Meteorological Society* 87 (3): 343–360. doi:10.1175/BAMS-87-3-343.

Mioduszewski, J. R., A. K. Rennermalm, D. A. Robinson, and L. Wang. 2015. "Controls on Spatial and Temporal Variability in Northern Hemisphere Terrestrial Snow Melt Timing, 1979-2012." *Journal of Climate* 28 (6): 2136–2153. doi:10.1175/JCLI-D-14-00558.1.

Mortin, J., S. E. L. Howell, L. Wang, C. Derksen, G. Svensson, R. G. Graversen, and T. M. Schrøder. 2014. "Extending the QuikSCAT Record of Seasonal Melt-Freeze Transitions over Arctic Sea Ice Using ASCAT." *Remote Sensing of Environment* 141. Elsevier Inc.: 214–230. doi:10.1016/j.rse.2013.11.004.

Mortin, J., T. M. Schrøder, A. W. Hansen, B. Holt, and K. C. McDonald. 2012. "Mapping of Seasonal Freeze-Thaw Transitions across the Pan-Arctic Land and Sea Ice Domains with Satellite Radar." *Journal of Geophysical Research: Oceans* 117 (C08004): C08004. doi:10.1029/2012JC008001.

Nghiem, S. V., and W.-Y.-Y. Tsai. 2001. "Global Snow Cover Monitoring with Spaceborne K U-Band Scatterometer." *Geoscience and Remote Sensing, IEEE Transactions On* 39 (10): 2118–2134. doi:10.1109/36.957275.

Ohmura, A. 2001. "Physical Basis for the Temperature-Based Melt-Index Method." *Journal of Applied Meteorology* 40: 753–761. doi:10.1175/1520-0450(2001)040<0753:PBFTTB>2.0.CO;2.

Raleigh, M. S., C. C. Landry, M. Hayashi, W. L. Quinton, and J. D. Lundquist. 2013. "Approximating Snow Surface Temperature from Standard Temperature and Humidity Data: New Possibilities for Snow Model and Remote Sensing Evaluation." *Water Resources Research* 49 (12): 8053–8069. doi:10.1002/2013WR013958.

Rotschky, G., T. V. Schuler, J. Haarpaintner, J. Kohler, and E. Isaksson. 2011. "Spatio-Temporal Variability of Snowmelt across Svalbard during the Period 2000-08 Derived from QuikSCAT/SeaWinds Scatterometry." *Polar Research* 30 (SUPPL.1): 1–15. doi:10.3402/polar.v30i0.5963.

Saito, K., T. Zhang, D. Yang, R. G. Sergei Marchenko, V. R. Barry, and L. D. Hinzman. 2013. "Influence of the Physical Terrestrial Arctic in the Eco-Climate System." *Ecological Applications* 23 (8): 1778–1797. doi:10.1890/11-1062.1.

Scherer, D., D. K. Hall, V. Hochschild, M. König, J.-G. Winther, and C. R. Duguay. 2005. "Remote Sensing of Snow Cover." *Remote Sensing in Northern Hydrology* 7–38. doi:10.1029/163GM03.

Shulski, M., and G. Wendler. 2007. *The Climate of Alaska*. Alaska: University of Alaska Press.

Stone, R. S., E. G. Dutton, J. M. Harris, and D. Longenecker. 2002. "Earlier Spring Snowmelt in Northern Alaska as an Indicator of Climate Change." *Journal of Geophysical Research: Atmospheres* 107: D10. doi:10.1029/2000JD000286.

Tang, Q., X. Zhang, and J. A. Francis. 2014. Extreme Summer Weather in Northern Mid-Latitudes Linked to a Vanishing Cryosphere. *Nature Climate Change* 4(1). Nature Publishing Group:45–50. doi:10.1038/nclimate2065.

Trusel, L. D., K. E. Frey, and S. B. Das. 2012. "Antarctic Surface Melting Dynamics: Enhanced Perspectives from Radar Scatterometer Data." *Journal of Geophysical Research: Earth Surface (2003–2012)* 117 (F2). doi:10.1029/2011JF002126.

Ulaby, F. T., R. K. Moore, A. K. Fung, and A. House. 1981. *Microwave Remote Sensing: Active and Passive*. Vol. 1. Massachusetts: Addison-Wesley Reading.

Ulaby, F. T., and W. H. Stiles. 1980. "The Active and Passive Microwave Response to Snow Parameters 2. Water Equivalent of Dry Snow." *Journal of Geophysical Research* 85 (C2): 1045–1049. doi:10.1029/JC085iC02p01045.

Urban, F. E., and G. D. Clow. 2014. "DOI/GTN-P Climate and Active-Layer Data Acquired in the National Petroleum Reserve–Alaska and the Arctic National Wildlife Refuge, 1998–2011." *U. G. Geological Survey Data Series 812*. http://pubs.usgs.gov/ds/812/introduction.html.

Wagner, W., S. Hahn, R. Kidd, T. Melzer, Z. Bartalis, S. Hasenauer, J. Figa-Saldaña, P. De Rosnay, A. Jann, and S. Schneider. 2013. "The ASCAT Soil Moisture Product: A Review of Its Specifications, Validation Results, and Emerging Applications." *Meteorologische Zeitschrift* 22 (1): 5–33. doi:10.1127/0941-2948/2013/0399.

Wang, L., C. Derksen, and R. D. Brown. 2008. "Detection of Pan-Arctic Terrestrial Snowmelt from QuikSCAT, 2000–2005." *Remote Sensing of Environment* 112 (10): 3794–3805. doi:10.1016/j.rse.2008.05.017.

Wang, L., C. Derksen, S. E. L. Howell, G. J. Wolken, M. Sharp, and T. Markus. 2009. "Integrated Pan-Arctic Melt Onset Detection from Satellite Microwave Measurements." In *66th Eastern Snow Conference*, 131–138.

Wendler, G., M. Shulski, and B. Moore. 2010. "Changes in the Climate of the Alaskan North Slope and the Ice Concentration of the Adjacent Beaufort Sea." *Theoretical and Applied Climatology* 99 (1–2): 67–74. doi:10.1007/s00704-009-0127-8.

WRCC. 2003. "Umiat, Alaska (509539): Period of Record Monthly Climate Summary." *Western Regional Climate Center*. www.wrcc.dri.edu.

Zhang, T., S. A. Bowling, and K. Stamnes. 1997. "Impact of the Atmosphere on Surface Radiative Fluxes and Snowmelt in the Artic and Subartic." *Journal of Geophysical Research* 102 (D4): 4287–4303. doi:10.1175/1520-0442(1996)009<2110:IOCOSR>2.0.CO;2.

Zhou, Z. Q., S. P. Xie, X. T. Zheng, Q. Liu, and H. Wang. 2014. "Global Warming-Induced Changes in El Niño Teleconnections over the North Pacific and North America." *Journal of Climate* 27 (24): 9050–9064. doi:10.1175/JCLI-D-14-00254.1.